Montreal, Canada, June 25–28, 2024

NEAR-WALL CHARACTERISTICS OF NON-EQUILIBRIUM TURBULENT BOUNDARY LAYERS ON ROUGH WALLS

Junlin Yuan
Department of Mechanical Engineering
Michigan State University
East Lansing, Michigan, USA
junlin@egr.msu.edu

Matthew Gatzek
Department of Mechanical Engineering
Michigan State University
East Lansing, Michigan, USA

Saurabh Pargal
Department of Mechanical Engineering
Michigan State University
East Lansing, Michigan, USA

ABSTRACT

Engineering models of rough-wall turbulent flows rely on reduced model of the near-wall layer of flow modified by roughness (i.e. the roughness sublayer) to provide boundary conditions to the flow above. It is important to understand how the sublayer responses to mean pressure gradient and its history for developing physics-based turbulence closures. This work examines characteristics of the roughness sublayer of two flat-plate turbulent boundary layers: one under strong non-equilibrium favorable pressure gradients using existing DNS data (Yuan and Piomelli, *J. Fluid Mech.* **780**:192-214, 2015) and the other under non-equilibrium adverse pressure gradients based on a roughness-resolved large-eddy simulation presented herein. The sublayer thickness is found to be constant in attached-flow regions, regardless of pressure gradients. When using a set of sublayer scales (U_R and y_R defined herein) to non-dimensionalize flow statistics, overall self-similar profiles of mean velocity, dispersive stress and constant total drag are observed. Results suggest the possibility of modeling the sublayer based on U_R-scaled statistics in non-equilibrium flows, in the context of sublayer-unresolved turbulence models.

INTRODUCTION

Surface roughness is present in a wide range of applications. In predictive engineering models of turbulent flows, such as Reynolds-averaged Navier-Stokes (RANS) models and wall-modeled large-eddy simulations (WMLES), roughness is usually not resolved, but instead its gross effects on the mean velocity and stresses are modeled. In such approaches, the roughness sublayer (RSL)—the layer where the mean flow is dynamically affected by roughness—is ignored. Instead, often the hydrodynamic drag of roughness (an integral of the total drag generated inside the RSL) and turbulence properties (turbulence kinetic energy, TKE, and Reynolds stresses, etc.) at the edge of the sublayer are used as boundary conditions of the layer above.

Since in most applications the surfaces are not flat or perfectly aligned with the freestream, pressure gradients are usually present in real flows and are often non-equilibrium. The inequilibrity in the bulk of the boundary layer has been modeled. However, most current roughness treatments assume canonical RSL in all cases and do not consider possible variations of the RSL under non-equilibrium pressure gradients (Volino *et al.*, 2022). Specifically, many roughness treatments prescribe $U(y)$ and turbulence quantities at the rough-wall boundary as fixed functions of k_s of the roughness, treated as a constitutive property of that surface. Examples include the k_s-based RANS model modification of Aupoix & Spalart (2003), the discrete element method (e.g. Taylor *et al.*, 1985), and the composite sublayer $U(y)$ profile model of Brereton *et al.* (2021). However, it is unclear how the sublayer flow, characterized by its thickness, drag generation and velocity statistics, depends on the streamwise pressure gradient and its history and whether existing RSL-flow models are extendible to non-equilibrium flows.

Most past numerical or experimental studies resolving the RSL focused on equilibrium wall-bounded flows, such as flat-plate boundary layers under zero-pressure gradients (ZPG) or fully-developed channel flows. Mangavelli & Yuan (2023) and Mangavelli *et al.* (2021) analyzed direct numerical simulations (DNS) of transient half-channel flows on rough walls, as they undergo non-equilibrium response to a step acceleration of the bulk velocity. Notably, they observed that the friction velocity $u_\tau(x)$ scales on the mean velocity at the edge of the RSL, $U_R(x)$, and not on the bulk velocity. In addition, the wake kinetic energy (WKE) accelerates at the pace of $U_R^2(x)$, while the TKE lags behind. These findings are similar to the observations of Yuan & Piomelli (2015) on a spatially developing flat-plate boundary layer under non-equilibrium favourable pressure gradients (FPG) on a rough wall. The results indicated that the drag coefficient of the roughness may be invariant in non-equilibrium accelerated flow when normalized appropriately, which is potentially useful in rough-wall turbulence modeling. Although a small number of studies were carried out focusing on the RSL in non-equilibrium accelerating flow, few are available on decelerating ones.

One objective of this work is to carry out a LES simulation of rough-wall flat-plate boundary layers with suction-and-blowing freestream, under strong adverse pressure gradients

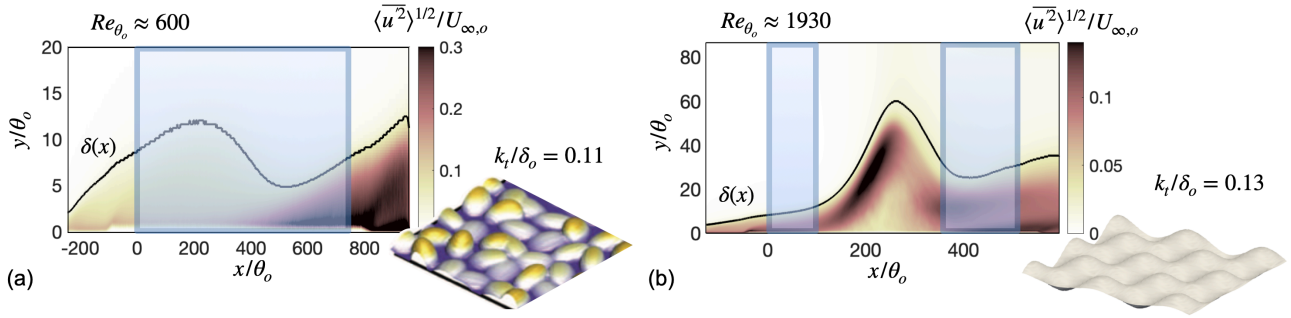

Figure 1. Boundary layer development of the FPG flow (a) and suction-blowing flow (b) shown using u' intensity. Boxes mark attached-flow regions examined in this work.

(APG) that lead to boundary layer separation, followed by a FPG region to force reattachment. Focus will be given to the attached flow regions . A second objective is to provide statistical comparison between the RSLs in FPG and APG flows. The existing FPG flow data of Yuan & Piomelli (2015) will be used for comparison. Since the minimum information needed from the RSL flow by a RSL-unresolved turbulence model (e.g. wall-modeled LES and RANS models) is the hydrodynamic drag and the RSL thickness (i.e. the near-wall region not to resolve in these types of models), the focus will be on these two quantities. Other quantities including the mean velocity, Reynolds stresses and dispersive stresses will also be discussed.

PROBLEM FORMULATION

The incompressible flow of a Newtonian fluid is governed by the equations of conservation of mass and momentum:

$$\frac{\partial u_i}{\partial x_i} = 0, \tag{1}$$

$$\frac{\partial u_j}{\partial t} + \frac{\partial u_i u_j}{\partial x_i} = -\frac{\partial P}{\partial x_j} - \frac{\partial \tau_{ij}}{\partial x_i} + \nu\nabla^2 u_j + f_j^{IB}, \tag{2}$$

where x_1, x_2 and x_3 (or x, y and z) are, respectively, the streamwise, wall-normal and spanwise directions, and u_j (or u, v and w) are the filtered velocity components in those directions; $P = p/\rho$ is the modified pressure, ρ the density and ν the kinematic viscosity. The term f_j^{IB} is a body force of the immersed boundary method used to impose non-slip/penetration boundary conditions at the roughness surface. The sub-filter stress τ_{ij} is modeled using a dynamic eddy-viscosity model (Germano *et al.*, 1991) based on the Lagrangian-averaging procedure. The governing equations are solved on a staggered grid using second-order central differences for all terms and second-order Adams-Bashforth semi-implicit time advancement. Double averaging is performed; $\overline{(\cdot)}$ and $\langle\cdot\rangle$ represent time averaging and intrinsic plane averaging, respectively. $\widetilde{(\cdot)}$ and $(\cdot)'$ represent form-induced and turbulent fluctuations.

The set-up of the boundary layer is similar to those of Wu & Piomelli (2018). Inlet turbulence is generated by the recycling and rescaling method (Lund *et al.*, 1998); a convective boundary condition (Orlanski, 1976) is used at the exit; a suction-blowing distribution of wall-normal velocity $V_\infty(x)$ is imposed on the top boundary to generate APG and downstream FPG regions in the boundary layer. The reference location ($x = 0$) is taken as the location where the rough-wall ZPG flow is fully developed. The momentum thickness (θ_o) and boundary layer edge velocity ($U_{e,o}$) at $x = 0$ are used as the reference length and velocity scales. At the reference location, $Re_\theta = 1930$. The domain lengths (normalized by θ_o) are 720, 86 and 75 in x, y and z. The numbers of grid points are 2560, 704 and 384 in these directions, respectively. This corresponds to $\Delta x^+ \leq 35$, $\Delta y^+_{min} \leq 0.6$ and $\Delta z^+ \leq 24$ throughout the boundary layer, and 13 and 19 points per roughness element in x and z, respectively. The resolution Δx_i^+ is comparable to existing LES studies of rough-wall flows (Wu & Piomelli, 2018; Yuan & Piomelli, 2014*a*).

On the bottom wall, a roughness different from the random sandgrains of Wu & Piomelli (2018) is used. A three-dimensional harmonic roughness (see Figure 1(b)) is imposed as $h(x,z) = (k_t/2)\cos[(2\pi/\lambda)x]\cos[(2\pi/\lambda)z] + k_t/2$, where h is the local elevation of roughness measured from the roughness trough which is taken as the bottom of the domain (i.e. $y = 0$), $k_t/\theta_o = 1.04$ is the peak-to-trough height (i.e. crest height), and $\lambda = k_t/0.28$ is the roughness wavelength. The use of a regular roughness allows performing local phase averaging to study detailed flow pattern inside the RSL in the future. $k_t/\delta \leq 0.13$ through out the domain (where δ is the boundary layer thickness). The roughness geometry corresponds to Case *60_424* of Chan *et al.* (2015), which has a threshold of fully rough regime of $k_t^+ \approx 50$ (measured in channel flows).

The FPG case (Yuan & Piomelli, 2015) is a DNS simulation with $Re_\theta = 600$ to 850. A sandgrain roughness is imposed on the wall (see Figure 1(a)), with k_t up to 0.11δ. An almost three-fold acceleration of streamwise freestream velocity is imposed at the top boundary. For both cases, Figure 1 displays the contours of $\langle\overline{u'^2}\rangle^{1/2}/U_{\infty,o}$ in both cases, showing the evolution of the boundary layer. δ is calculated based on a threshold of $\langle\overline{u'^2}\rangle^{1/2}/U_{\infty,o} = 0.03$. In the suction-blowing case, a separation bubble is formed with a separation point at $(x - x_o)/\theta_o \approx 110$. The results discussion is focused on the attached flow region highlighted in Figure 1: $(x - x_o)/\theta_o \in [0, 90]$ and $(x - x_o)/\theta_o \in [360, 500]$ for the suction-blowing flow and $(x - x_o)/\theta_o \in [0, 750]$ for the FPG flow. The minimum and maximum values of $(x - x_o)/\theta_o$ of these regions are selected such as the boundary effects (i.e. graduate change of roughness height toward smooth-wall condition at domain inlet and outlet) are negligible.

RESULTS

First, the strength of pressure gradients of the two cases in the attached flow regions are quantified, using parameters $K = (\nu/U_e^2)U_e'$ and $\beta = (\delta^*/\tau_w)P_e'$, where $\tau_w(x) = \int \overline{f_1^{IB}}(x,y,z)dydz$. Both parameters show that strong pressure gradients are reached, in both signs. The non-constant val-

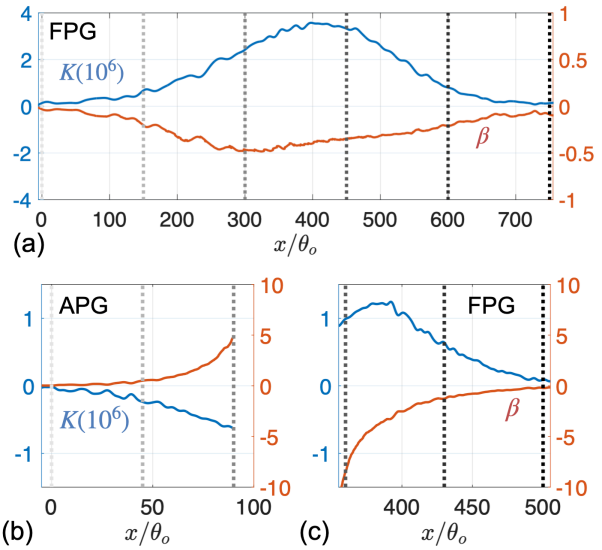

Figure 2. Streamwise variations of dimensionless pressure gradients (K and β) in the FPG (a) and suction-blowing cases (b,c). ---- x locations for statistical studies in this work.

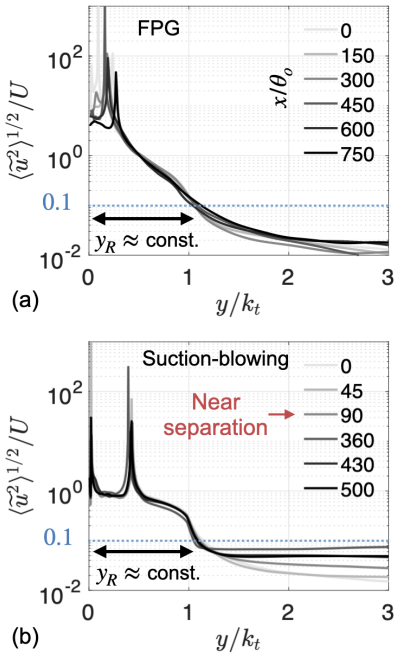

Figure 3. Determination of roughness sublayer thickness (y_R, above which $\langle\widetilde{u}^2\rangle^{1/2}/U < 0.1$) in the two cases.

ues show that the boundary layer is strongly non-equilibrium. The variation of k_t^+ (to be shown in Figure 5(b)) indicates that the suction-blowing flow is fully rough at $x = 0$. As k_t^+ decreases along x due to a decrease of u_τ approaching the separation point, the flow becomes nominally transitionally rough at $(x-x_o)/\theta_o \approx 100$. For the FPG flow, Yuan & Piomelli (2015) showed that the sandgrain roughness reaches fully rough regime at $k_t^+ \approx 90$ in channel flows. Figure 5(a) shows that the flow is transitionally rough at $(x-x_o)/\theta_o = 0$ and becomes nominally fully rough at $(x-x_o)/\theta_o \approx 430$.

To characterize the RSL, first the sublayer thickness (y_R) is quantified. The RSL, i.e. the layer below y_R, is defined as the layer in which the turbulent flow displays spatial het-

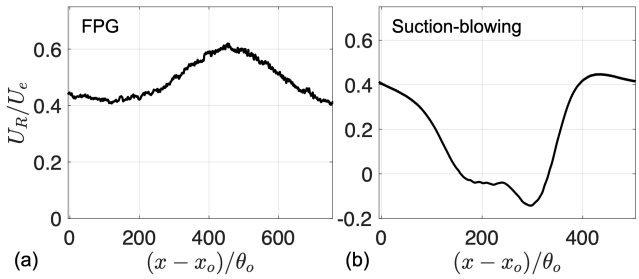

Figure 4. Streamwise development of the RSL velocity scale $U_R(x)$, normalized by local $U_e(x)$, in the two cases.

erogeneities due to the presence of roughness (Pokrajac *et al.*, 2007): $\langle\widetilde{u}^2\rangle^{1/2}(y)/\langle\overline{u}\rangle(y) \geq \gamma$, where threshold γ is a small value, taken as 0.1 herein. Figure 3(a) plots the wall-normal profile of $\langle\widetilde{u}^2\rangle^{1/2}/\langle\overline{u}\rangle$ at various x locations (with darker line color indicating increasing x). Logarithmic scaling is used in the vertical axis for a clear comparison. The specific profile shape inside the RSL are not the same between the two cases, since the roughness geometries are different. It was checked that various γ values from 0.15 to 0.3 do not lead to a significant change in the calculated thickness. It is shown that the $y_R \approx k_t$ and that y_R varies only weakly on x (indicating a weak dependence on pressure gradient), even for the nominally transitionally rough regions: $(x-x_o)/\theta_o = 0$ for FPG flow and $(x-x_o)/\theta_o = 90$ near the separation point for the suction-blowing flow. In studies of temporally accelerating flows (Mangavelli *et al.*, 2021), the RSL thicknesses calculated in similar ways were also shown to be independent of time, for different roughness geometries. Therefore, the invariant RSL extent in non-equilibrium boundary layers appears to be robust.

Based on y_R, a RSL velocity scale, i.e. the RSL edge velocity, can be defined: $U_R(x) \equiv \langle\overline{u}\rangle(x, y_R)$. The variation of $U_R(x)$ is plotted in Figure 4 for the two cases. Here, $U_R(x)$ is calculated as $U(x, y_{R,o})$, where $y_{R,o}$ is the RSL thickness at the reference x location. The choice of using a fixed y location to evaluate U_R arises from the observation that y_R is constant in the attached flow region; using the local $y_R(x)$ to evaluate U_R instead faces challenges in the detachment region where the dispersive stress profile departs significantly from those shown in Figure 3(b), rending it difficult to quantify $y_R(x)$ there. Figure 4 shows that, in the FPG boundary layer, U_R increases faster than U_e during flow acceleration, while in the APG region of the suction-blowing case it decrease faster than U_e. These are signatures of the non-equilibrium boundary layers. In the detachment region shown in Figure 4(b), U_R is negative, indicating reverse flow near the roughness crests. The asynchronous variations of U_R and U_e suggests that U_R may be a better velocity scale for the flow near the rough wall; this point is to be demonstrated next.

In accelerated channel flows (Mangavelli *et al.*, 2021), $\tau_w(x)$ was found to scale approximately on $U_R(x)^2$. Figure 5 compares the streamwise evolutions of the drag coefficients obtained based on U_R or U_e for the two cases, together with the variation of k_t^+. The scaling of τ_w on U_R^2 is shown to be also true in the present spatially developing boundary layers in the region with high k_t^+, by the hydrodynamic drag coefficient based on U_R, $C_{D,R} = \tau_w/(1/2\rho U_R^2)$, which takes an almost constant value in the FPG flow and in the suction-blowing flow sufficiently far from the separation zone (i.e. the zone with $\tau_w(x) < 0$). On the other hand, τ_w does not scale on U_e^2 in either of the flows, as shown by the significantly varying

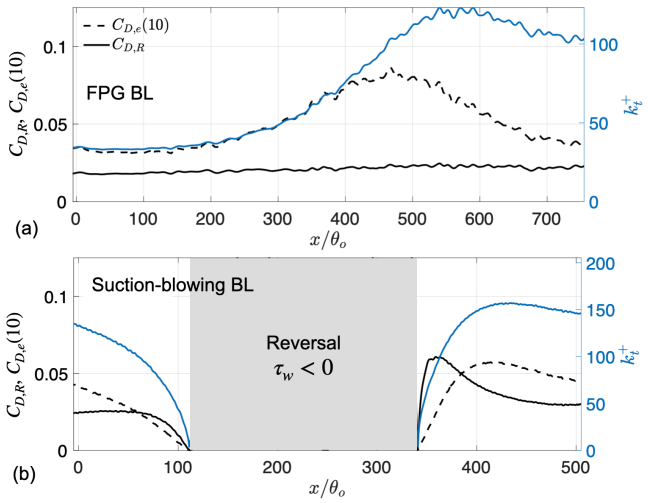

Figure 5. Streamwise variations of drag coefficients based on U_R or U_e, compared to the variation of k_t^+ in both cases.

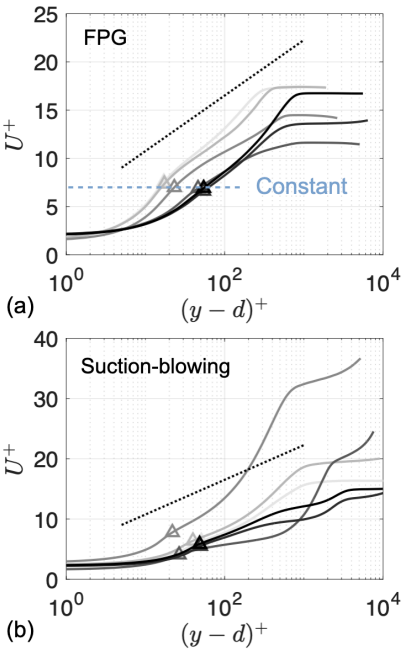

Figure 6. Streamwise mean velocity profiles in viscous units. --- $U^+ = (1/\kappa)\log(y-d)^+ + B$ with $\kappa = 0.4$ and $B = 5.0$.

$C_{D,e} = \tau_w/(1/2\rho U_e^2)$. This observation suggests that, when $y_R^+ \gg 1$, the drag coefficient (when defined appropriately) is invariant with the imposed streamwise pressure gradient and its history.

Figure 6 shows the double-averaged velocity profiles in viscous scaling in the two cases. Here, the y axis is offset by the amount of virtual origin d—defined as the distance from the trough elevation ($y = 0$) to the centroid of the y-profile of the total drag distribution $\langle \overline{f_1^{IB}} \rangle_o(y)$ (Jackson, 1981) to collapse the log-law layer. Yuan & Piomelli (2015) discussed the U^+ profile variation under strong FPG on the rough wall, characterized by an augmentation of the U^+ offset in the logarithmic layer and a milder log-law slope similar to a smooth-wall boundary layer under FPG. The higher offset is consistent with the increase of τ_w. On the other hand, in the separated boundary layer a strong wake is observed as a result of the APG when

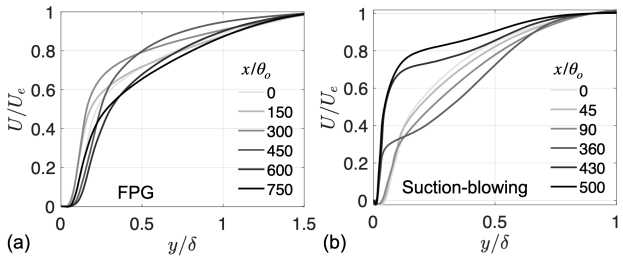

Figure 7. $U(x,y)$ profiles normalized by local U_e.

x moves toward the separation point, together with a decrease of logarithmic offset due to a decrease of τ_w. After reattachment before $(x-x_o)/\theta_o = 360$, the augmented wake reduces along x toward the equilibrium state. These observations are consistent with those of Wu & Piomelli (2018) for a sandgrain roughness. In addition, the scaling of hydrodynamic drag on U_R^2 as observed above indicates that U_R, when evaluated in plus units, stays approximately constant in attached flows, as $U^+(y_R) \sim 1/\sqrt{C_{D,R}}$, where $C_{D,R}$ is approximately a constant. The y_R locations of the U profiles are marked by triangles in Figure 6. For the FPG case, indeed an almost constant $U^+(y_R)$ value is shown for all x locations. For the suction-blowing case, some variation is observed right before the separation and right after the reattachment (as shown by the profiles at $(x-x_o)/\theta_o = 90$ and 360), consistent with the variation of $C_{D,R}(x)$ in these regions as shown in Figure 5(b).

The scalings of the RSL flow statistics including mean velocities, Reynolds stresses and dispersive stresses are analyzed next. First, $U(y)$ is plotted using the outer scalings (local values of U_e and δ) in Figure 7 for the two cases in the attached-flow x locations. The profiles at different x do not collapse in any part of the boundary layer. The RSL region (i.e. $y_R/\delta < 0.1$) is characterized by reduction of momentum due to the total drag imposed by roughness. Figure 7(a) shows that acceleration leads to a fuller profile with stronger shear near the wall, explaining the faster increase of U_R than that of U_e (shown in Figure 4), while the opposite is shown in the APG flow in Figure 7(b).

When U_R and y_R are used as scaling variations to non-dimensionalize U and y (as shown in Figure 8), however, a near-wall collapse is found. Due to the normalization, all profiles pass through points $(0,0)$ and $(1,1)$. This allows a better collapse of data in the RSL (i.e. region of $y/y_R \in [0,1]$). Surprisingly, the velocity profile shape in RSL is shown to vary only weakly in the present strongly non-equilibrium boundary layers, even in the regions near the separation bubble ($(x-x_o)/\theta_o = 90$ and 360 in Figure 8(d)). Slight change of profile shape is observed in the FPG flow shown in Figure 8(b), which may be explained by a transition from the nominally transitionally rough to the fully rough state. It is unclear why this weak dependency is not observed for the sinusoidal roughness (Figure 8(d)); a roughness-geometry effect may be present and future work should investigate FPG flow with the same roughness geometry. The self-similarity of $U(y)$ inside the RSL when normalized using the RSL scales is a significant finding, as it suggests that models of the RSL velocity developed using equilibrium-flow data (e.g. the composite profile model of Brereton *et al.* (2021)) may be directly extendible to non-equilibrium boundary layers.

To examine the overall development of the dispersive stresses, the y-profiles of WKE (defined as $\langle \widetilde{u}_i \widetilde{u}_i \rangle/2$) in the attached-flow regions are plotted in Figure 9, normalized by U_e or U_R. Here y is normalized by $k_t \approx y_R$. The WKE is

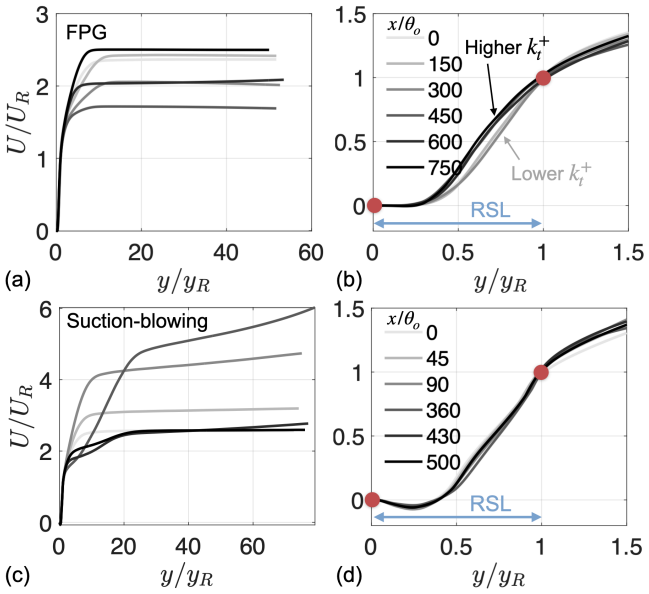

Figure 8. $U(x,y)$ normalized by local U_R and y_R: full profiles in (a,c); zoomed-in plots in (b,d) to show the collapse in RSL. ○ Points that all profiles pass through due to the normalization.

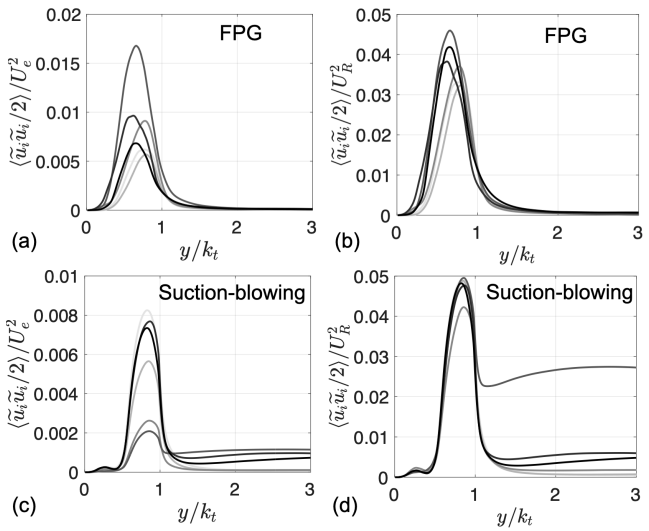

Figure 9. Wake kinetic energy normalized by U_e^2 (a,c) and U_R^2 (b,d).

strong in the region around $y/k_t < 1$ only, due to the definition of RSL based on locally significant dispersive stress and the fact that $k_t \approx y_R$ as found for the present flows. Figure 9(a,c) shows that the WKE does not accelerate or decelerate at the same pace as $U_e(x)$. Instead, a freestream acceleration (or deceleration) leads to more rapid increase (or decrease) of dispersive perturbation than the freestream itself. Figure 9(b,d) shows that the WKE profile inside the RSL scales largely with U_R^2 instead. This finding was first observed by Yuan & Piomelli (2015) for the FPG flow; this work shows that the same applies to the present separated and reattached flows. As $\widetilde{u}_i$ fields have an important role in producing turbulence in rough-wall flows (Yuan & Piomelli, 2014*b*), in particular for the non-equilibrium ones (Mangavelli *et al.*, 2021), the result suggests some level of self-similarity in the turbulence production process despite the non-equilibrium pressure gradients.

Lastly, the streamwise development of the y-profiles of

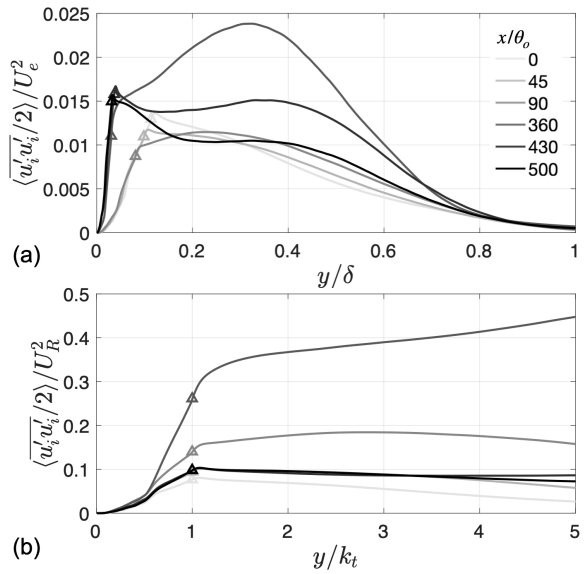

Figure 10. Turbulent kinetic energy in the suction-blowing case normalized by U_e^2 (a) and U_R^2 (b). △ Elevation $y/k_t = 1$.

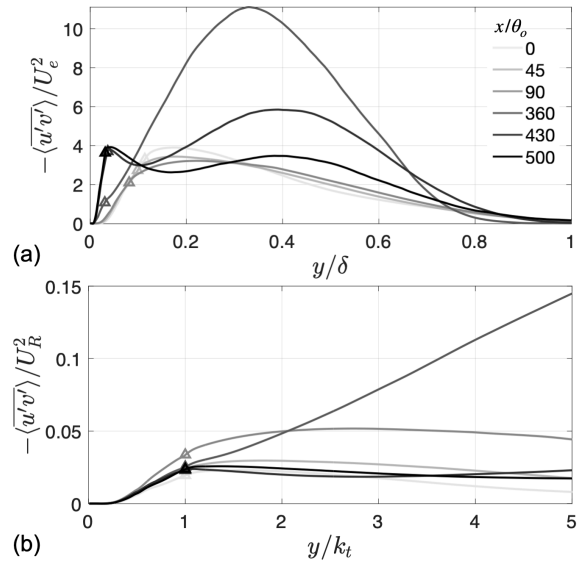

Figure 11. Reynolds shear stress magnitude in the suction-blowing case normalized by U_e^2 (a) and U_R^2 (b). △ Elevation $y/k_t = 1$.

Reynolds stresses are analyzed for the suction-blowing case, focusing on the turbulent kinetic energy in Figure 10 and the Reynolds shear stress in Figure 11. The extent of the RSL is marked with triangles, which approximately coincide with the near-wall peak of TKE signifying the TKE production due to roughness. Figure 10 shows that the near-wall TKE do not perfectly scale with either the outer or RSL velocity scale, but the TKE value displays less variation when normalized with the outer scale. This can be explained by the dominant contribution from the streamwise Reynolds stress, which is attributed mostly to the large energetic motions that extend to the outer layer.

On the other hand, the Reynolds shear stress inside the RSL (i.e. y/k_t less than around 1) is shown to be better collapsed by the RSL velocity scale (Figure 11(b)), compared to that normalized using the edge velocity. Strikingly, profiles in

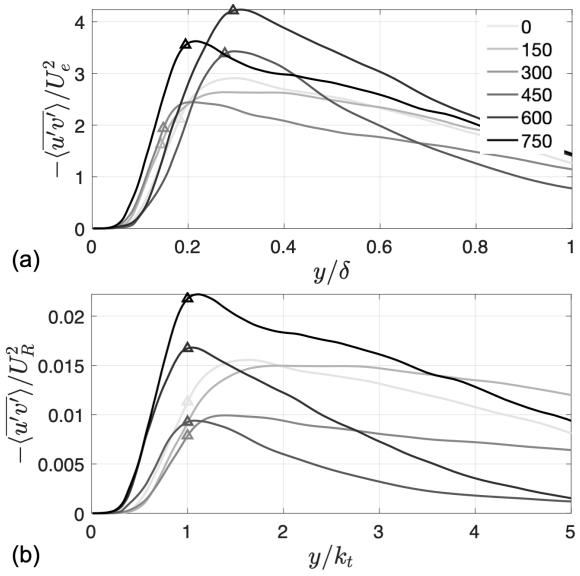

Figure 12. Reynolds shear stress magnitude in the FPG case normalized by U_e^2 (a) and U_R^2 (b). $\triangle$ Elevation $y/k_t = 1$.

the region downstream from the reattachment point (i.e. those at $(x-x_o)/\theta_o = 360$, 430 and 500) collapse very well in the RSL under U_R^2 scaling; outside the RSL the profiles differ, due to the lower $U_R(x)$ values near the separation bubble. These observation suggests that, although the ensemble of turbulent motions inside the RSL do not scale with U_R, the active motions responsible of turbulence production do.

However, the above observation on the self-similarity of Reynolds shear stress normalized using U_R (as shown in the region downstream of reattachment) does not apply to the FPG case with sandgrain roughness, as shown in Figure 12(b). This is apparent especially in the region $(x-x_o)/\theta_o \in (450, 750)$ where the FPG flow recovers toward the downstream ZPG flow. It is not clear at this point whether this reflects an effect of roughness geometry or that of the pressure-gradient history.

Conclusions

Two non-equilibrium spatially developing boundary layers over rough walls are compared, with the focus on the roughness sublayer (RSL) characteristics and flow statistics in attached flows. Comparisons are made on how weak to strong non-equilibrium pressure gradients (in both signs) affect rough-wall boundary layer development and the RSL flow statistics. Results show that, regardless of the magnitude, direction and history of the mean streamwise pressure gradients, some flow properties in the RSL remain self-similar or invariant when normalized using the RSL scales: the RSL thickness (y_R) and the mean streamwise velocity at the edge of the sublayer (U_R). These properties include the total drag, mean streamwise velocity and dispersive stresses. The RSL thickness is also invariant in attached flows. In some scenarios the RSL Reynolds shear stress also display self-similarity to some extent, but the Reynolds stress dependencies are more complex and need further explanation, possibly based on Reynolds stress budget. These results provide insights for developing physics-based turbulence closures that do not resolve the roughness sublayer. Future work will explore scalings for individual terms responsible for the convection, production and dissipation of Reynolds stresses and their anisotropy.

Acknowledgements

The authors acknowledge the financial support of the Office of Naval Research (award number N00014-17-1-2102). MG is currently affiliated with CFD Research Corporation (USA). SP is currently affiliated with Cummins Inc. (USA).

REFERENCES

Aupoix, B. & Spalart, P. R. 2003 Extensions of the spalart–allmaras turbulence model to account for wall roughness. *Int. J. Heat Fluid Flow* **24**, 454–462.

Brereton, G. J., Aghaei Jouybari, M. & Yuan, J. 2021 Towards modeling of turbulent flow over surfaces of arbitrary roughness. *Phys. Fluids* **33**, 065121–1—13.

Chan, L., MacDonald, M., Chung, D., Hutchins, N. & Ooi, A. 2015 A systematic investigation of roughness height and wavelength in turbulent pipe flow in the transitionally rough regime. *J. Fluid Mech.* **771**, 743–777.

Germano, M., Piomelli, U., Moin, P. & Cabot, W. H. 1991 A dynamic subgrid-scale eddy viscosity model. *Phys. Fluids A* **3**, 1760–1765.

Jackson, P. S. 1981 On the displacement height in the logarithmic velocity profile. *J. Fluid Mech.* **111**, 15–25.

Lund, T. S., Wu, X. & Squires, K. D. 1998 Generation of inflow data for spatially-developing boundary layer simulations. *J. Comput. Phys.* **140**, 233–258.

Mangavelli, S. C. & Yuan, J. 2023 Effects of form-induced velocity in rough-wall turbulent channel flows. *J. Turbul.* **24**, 14–35.

Mangavelli, S. C., Yuan, J. & Brereton, G. J. 2021 Effects of surface roughness topography in transient channel flows. *J. Turbul.* **22**, 434–460.

Orlanski, I. 1976 A simple boundary condition for unbounded hyperbolic flows. *J. Comput. Phys.* **21**, 251–269.

Pokrajac, D., Campbell, L. J., Nikora, V. & Manes, C. adn McEwan, I. 2007 Quadrant analysis of persistent spatial velocity perturbations over square-bar roughness. *Exp. Fluids* **42**, 413–423.

Taylor, R. P., Coleman, H. W. & Hodge, B. K. 1985 Prediction of turbulent rough-wall skin friction using a discrete element approach. *J. Fluids Eng.* **107**, 251–257.

Volino, R. J., Devenport, W. J. & Piomelli, U. 2022 Questions on the effects of roughness and its analysis in non-equilibrium flows. *J. Turbul.* **23**, 454–466.

Wu, W. & Piomelli, U. 2018 Effects of surface roughness on a separating turbulent boundary layer. *J. Fluid Mech.* **841**, 552–580.

Yuan, J. & Piomelli, U. 2014*a* Estimation and prediction of the roughness function on realistic surfaces. *J. Turbul.* **15**, 350–365.

Yuan, J. & Piomelli, U. 2014*b* Roughness effects on the Reynolds stress budgets in near-wall turbulence. *J. Fluid Mech.* **760**, R1.

Yuan, J. & Piomelli, U. 2015 Numerical simulation of a spatially developing accelerating boundary layer over roughness. *J. Fluid Mech.* **780**, 192–214.